Rev.2

CRYSTAL CHEMISTRY AND SURFACE CONFIGURATIONS OF TWO POLYLITHIONITE-1*M* CRYSTALS

Chiara Elmi[1], Maria Franca Brigatti[1], Stephen Guggenheim[2], Luca Pasquali[3,4], Monica Montecchi[3,4], and Stefano Nannarone[3,4]

[1]Dipartimento di Scienze Chimiche e Geologiche, Università di Modena e Reggio Emilia, Largo S. Eufemia 19, 41121 Modena, Italy; [2]Department of Earth and Environmental Sciences, University of Illinois at Chicago, 845 West Taylor Street, Chicago, Illinois, 60607-7059, U.S.A.; [3]Dipartimento di Ingegneria "Enzo Ferrari", Università di Modena e Reggio Emilia, Via Vignolese 905, 41125 Modena, Italy;[4] IOM INFM-CNR Area Science Park, Building MM, S.S. 14, Km 163.5, 34012, Basovizza (TS), Italy

Abstract – This paper explores the crystal chemical features of the bulk and the outermost (001) surface layers of two trioctahedral Li-rich mica-1*M* (space group *C*2) polytypes, *i.e.* a polylithionite (MLG-114) from Li-mica granitic pegmatite at St. Austell (SW England) and a Fe^{2+}-rich polylithionite (Ch-140) from a rhyolite at Profitis Ilias, Chios Island, Greece. Structural formulae are $^{[xii]}(K_{0.952}Na_{0.019}Rb_{0.019})\ ^{[vi]}(Al_{1.034}Li_{1.459}Fe^{2+}_{0.389}Fe^{3+}_{0.046}Mn_{0.038}Mg_{0.002}Zn_{0.002}Ti_{0.001})\ ^{[iv]}(Al^{3+}_{0.477}Si_{3.523})O_{10.081}(F_{1.735}OH_{0.184})$ and $^{[xii]}(K_{0.992}Na_{0.014})\ ^{[vi]}(Al_{0.980}Li_{1.028}Fe^{2+}_{0.787}Fe^{3+}_{0.022}Mn_{0.059}Mg_{0.052}Zn_{0.010}Ti_{0.024})\ ^{[iv]}(Al^{3+}_{0.857}Si_{3.143})\ O_{10.095}\ (F_{1.617}\ OH_{0.288})$ for MLG-114 and Ch-140, respectively. Each mineral is characterized by a high F content in the anion site and has tetrahedral and octahedral compositions related to the exchange vector $^{[vi]}Li_{-1}{}^{[iv]}Si_{-1}\ ^{[vi]}Fe^{2+}\ ^{[iv]}Al$. Unit cell dimensions are a = 5.251(1), b = 9.066(2), c = 10.087(2) Å; β = 100.694(5)° for polylithionite MLG-114 and a = 5.282(1), b = 9.121(3), c = 10.080(3) Å; β = 100.764(5)° for Ch-140. Crystal structure refinements (agreement factors are R = 3.58% and R = 3.75% for MLG-114 and Ch-140, respectively) demonstrate that the $^{[vi]}Li_{-1}{}^{[vi]}Fe^{2+}\ ^{[iv]}Si_{-1}{}^{[iv]}Al$ exchange vector produces a decrease in the lateral dimensions of the tetrahedral and octahedral sheets. The decrease in basal oxygen distances results from the effect of the strain caused by the orientation of opposing tetrahedral sheets within a 2:1 layer. The decrease reduces the strain so that the basal oxygen plane can remain nearly planar. Changes in these dimensions via distortions of the tetrahedral basal-oxygen ring (α = 3.3° and α = 4.1° for MLG-114 and Ch-140, respectively) are limited. Octahedral M1 and M3 sites are similar in size and much larger than M2 and the mean electron count is M3 < M1 < M2 in MLG-114 and M1 ≅ M2 < M3 in Ch-140. Al preferentially occupies the M2 site, whereas Fe and Li

Always consult and cite the final, published document. See http://www.minsocam.org or GeoscienceWorld

are nearly disordered between M1 and M3 sites with a slight preference of Fe for the M1 site in MLG-114 and for M3 site in Ch-140.

Element concentrations on the (001) surface, obtained through X-ray photoelectron spectroscopy (XPS) high-resolution spectra for Si_{2p}, Al_{2p}, Fe_{2p}, K_{2p}, Li_{1s}, and F_{1s} core levels, indicates that a greater amount of lithium and a smaller amount of potassium characterize the surface with respect to the bulk. The decrease in K content, commonly observed in micas, is related to its location on the cleavage surface, because the cation must be distributed equally between the two (001) surfaces generated upon cleavage. The increase in Li content on or near the (001) cleavage surface suggests a preference for cleavage near lithium-enriched regions. The surface structure of the polylithionite crystals suggests that Al, Li, and Fe cations maintain coordination features at the surface similar to the bulk. Silicon, however, which is generally in four-fold coordination, shows also a small number of [1]-fold coordinated components at a binding energy of 99.85 eV.

Key Words – Polylithionite, crystal chemistry, crystal structure, surface features

Corresponding author: S. Guggenheim, xtal@uic.edu

INTRODUCTION

Mineral-surface science over the last few years has evolved into research fields that provide a better understanding not only of how mineral surfaces affect the environment, but also how mineral surfaces may be utilized to advance applications in industrial processes (*e.g.*, Hochella Jr, 1995; Maurice, 2009). For example, a satin or "pearlescent" luster occurs by using mica flakes (transparent layers) and TiO_2 coatings to produce optical effects relating to the differences in refractive indices of the component layers, boundary interactions and optical interference, and the angles of viewing. Tenório Cavalcante et al. (2007) found that pearlescence in manufactured ceramics can be stable to fired temperatures as high as 1200 °C in certain circumstances.

The near-surface regions of Earth (where anthropogenic influence is important) are dynamic systems. Many natural processes (*e.g.*, weathering, sorption) associated with changes in these systems occur at the mineral surface. Near the Earth's surface, finely divided clay minerals are the dominant phyllosilicates, but because clay minerals may be very fine grained, this property makes the direct study of their surfaces difficult. In contrast, large flakes of micas can more easily be investigated, and there is a general agreement that micas may be useful as an analogue for the behavior of clay surfaces. Phyllosilicate surfaces, in part, influence groundwater chemistry, sorption and desorption of organic and inorganic compounds, retardation of transport of radiogenic isotopes

Always consult and cite the final, published document. See http://www.minsocam.org or GeoscienceWorld

and heavy metal pollutants, etc. In addition, the study of phyllosilicate surfaces is also important in weathering of rock, soil formation, and oil-reservoir behavior. Mineral surface properties, especially those of phyllosilicates, are often atomically similar to the uppermost layers of the bulk, but may be different (*i.e.*, redox state, atomic coordination, type of chemical bonds, etc.) from the bulk structure at greater depths below the mineral surface.

Polylithionite is the Li-rich end member in the polylithionite [$KLi_2AlSi_4O_{10}(F,OH)_2$] - siderophyllite [$KFe^{2+}{}_2Al(Al_2Si_2)O_{10}(F,OH)_2$] join, as defined by the exchange vector $^{[iv]}Si^{4+}{}_{-1}\,^{[vi]}Li_{-1}\,^{[iv]}Al\,^{[vi]}Fe^{2+}$ (Rieder et al. 1998). In lithian mica-1*M*, the octahedral sheet contains three different cations: Li^{1+}, Fe^{2+}, and Al^{3+}, together with other minor substitutions. Li-enrichment in trioctahedral micas may produce crystal structural features, such as cation ordering with the much larger Li^{1+} and Fe^{2+} cations occupying the *trans* (M1) sites and one of the *cis*-oriented octahedral sites (usually, M3) and Al^{3+} occupying one of the *cis*-sites (commonly, M2) (Guggenheim and Bailey 1977; Guggenheim 1981; Bailey 1984; Brigatti and Guggenheim 2002).

The octahedral-site mean bond length is ⟨M1-O⟩ ≅ ⟨M3-O⟩ > ⟨M2-O⟩ and occasionally ⟨M1-O⟩ ≅ ⟨M2-O⟩ > ⟨M3-O⟩ (Guggenheim 1981; Backhaus 1983; Brigatti et al. 2000). The scattering efficiency for M1, M2, and M3 sites also implies ordering with M1 ≠ M2 ≠ M3, M1 ≅ M3 > M2, or M1 ≅ M2 > M3. These features involve a reduction from ideal symmetry of *C*2/*m* to *C*2 space group, in particular, referring to OD-interpretation, from *C*12/*m*(1) to *C*12(1) (Dornberger-Schiff et al. 1982).

Structural refinements show an octahedral coordination for Li (for a review see Brigatti and Guggenheim 2002). However, Robert and Volfiger (1979) and Robert et al. (1993) suggested that, in synthetic trioctahedral micas, Li may exchange for K in interlayer sites with Li located in the interlayer in a pseudo-octahedral cavity.

Using angle-dependent XANES (AXANES) potassium K-edge spectra via synchrotron radiation on polylithionite-siderophyllite trioctahedral 1*M*-micas, Cibin et al. (2010) examined the contributions arising from multiple-scattering interactions of the photoelectron ejected from the potassium absorber. The data reflected: i) the interactions with near- and next-nearest neighboring oxygen atoms lying on the basal planes of the tetrahedral sheets; ii) the octahedral cation ordering; and iii) the F for OH substitution of the anion site. Pini et al. (2012) found that in Fe-rich lithian micas, the temperature where the maximum in magnetic susceptibility occurs is strongly affected by Fe octahedral ordering, thus imparting unique properties for these micas.

The atomic arrangement of the bulk and surface of polylithionite crystals showing different $^{[vi]}(Li+Al)/^{[vi]}(Li+Al+Fe^{2+})$ ratios can be significantly informative in understanding the octahedral

Always consult and cite the final, published document. See http://www.minsocam.org or GeoscienceWorld

cation distribution (clustering or random distribution) and its effect on the surface structure as well as on the crystal structural mechanisms affecting the polylithionite-siderophyllite join.

This study compares the crystal structural and chemical data for the bulk and the surface of two 1*M* polytypes on the polylithionite-siderophyllite join. These micas display important differences in the $^{[6]}(Li+Al)/^{[6]}(Li+Al+Fe^{2+})$ ratio. The micas include a polylithionite from a Li-mica granitic pegmatite unit at St. Austell (SW England) and a Fe-rich polylithionite close to the polylithionite-siderophyllite boundary (Fig. 1) from the rhyolite of Profitis Ilias, located at the SE coast of Chios Island, (NE part of Aegean Sea, Greece).

EXPERIMENTAL METHODS

Samples

Most publications (*e.g.*, Cundy et al. 1960; Henderson et al. 1989) on the chemistry and petrology of the St. Austell granite have noted the occurrence of lithium-bearing micas in the district. The St. Austell granite is fine-to medium-grained with quartz, alkali feldspar, plagioclase, and topaz. The granite consists of three units: i) biotite granite; ii) pegmatitic Li-mica granite; and iii) finer grained Li-mica granite. Li-micas are primary or formed under sub-solidus conditions during the earliest stages of hydrothermal activity (Henderson et al. 1989). The Li-mica granites are readily distinguished from the biotite granites by the occurrence of micas along the polylithionite-siderophyllite join. Both the topaz and lithian micas are F-rich. The polylithionite (MLG-114) considered in this study is a pale, pink-brown, primary phenocryst from the pegmatitic Li-mica granite unit with crystals ranging from 2 to 5 mm in diameter.

The Chios Island micas are primary products of rhyolite of Profitis Ilias together with feldspars (sanidine and plagioclase), quartz, and garnets (Mitropoulos et al. 1999). The euhedral mica phenocrysts of Fe-polylithionite (Ch-140) studied here are pale brown in color with a range in diameter from 2 to 7 mm.

Chemical composition and calculation of the chemical formula

Chemical composition (Table 1) of both samples was determined on several crystal fragments with a Cameca SX 50 electron microprobe. The following operating conditions were applied: accelerating voltage 20 kV, sample current 20 nA, and defocused beam diameter 4 μm. The following standards were used: orthoclase (K), albite (Na), hematite (Fe), diopside (Si), $MnTiO_3$ (Mn, Ti), Al_2O_3 (Al), MgO (Mg), CaF_2 (F), sphalerite (Zn) and synthetic Rb-rich glass (Rb). The F content was determined from the method reported by Foley (1989). No evidence of volatilization of

Always consult and cite the final, published document. See http://www.minsocam.org or GeoscienceWorld

F was observed. Analyses of more than 9 points on each fragment showed sample homogeneity and produced a statistically significant average. FeO determination followed the procedure by Meyrowitz (1970).

The Li content was determined via laser ablation inductively coupled to plasma mass spectroscopy (LA-ICP-MS, UP 213, New Wave Research), where the ablated material was transported to the quadrupole ICP-MS XSeriesII, supplied by Thermo Fischer Scientific. Three line scans, traced along the entire crystal and taken at three different points over a 60 μm spot at a scan speed of 25 μm/s, were performed. The dwell time was set at 20 s. The ablation frequency was 10 Hertz in all scans. The ablated aerosol was atomized at 0.68 bar into the plasma of the ICP-MS unit. The standard reference used to create the calibration curve was NIST 612 (a synthetic glass trace-element reference standard). ^{29}Si was selected as the internal standard. The data obtained were then normalized to the sample SiO_2 content, as measured via electron microprobe analysis. The $(OH)^-$ content was derived from thermo-gravimetric analysis in He gas flow using a Seiko SSC 5200 thermal analyzer (heating rate 10 °C/min and gas flow rate 100 μl/min), equipped with a mass spectrometer (GeneSys ESS, Quadstar 422).

The chemical formula was calculated by an iterative approach. As a first step, the charges of cations in tetrahedral, octahedral and interlayer sites were set equal to 22. The composition of the anion site, populated by OH, F and O, was a result of this step. Given X = 2-(OH+F), the chemical formula was thus calculated assuming 22+X positive charges for tetrahedral, interlayer and octahedral sites, which leads to an assessment of anion composition and therefore to a value for X. The iterative procedure was used until the difference in the X value from each step, was $< 10^{-7}$ in magnitude.

Single-crystal X-ray diffraction data

Each crystal was mounted on a Bruker X8-Apex fully automated four-circle diffractometer with Kappa geometry, equipped with a fine focus Mo ceramic X-ray tube ($\lambda = 0.7107$ Å) and APEX 4K CCD detector. The data collection strategy was obtained using the APEX2 software. Preliminary lattice parameters and an orientation matrix were obtained from three sets of frames and refined during the integration process of intensity data. Diffraction data were collected with ω scans at specific φ settings (φ–ω scan). Data were processed using SAINT Plus (Bruker 2003). The SADABS package (Sheldrick 1996) was used to perform a semi-empirical absorption correction. Space group determination and data merging were performed using XPREP (Sheldrick 1997). The crystal structure was refined with the SHELX-97 package of programs (Sheldrick 1997).

Always consult and cite the final, published document. See http://www.minsocam.org or GeoscienceWorld

Surface measurements

Chemical analyses of the (001) surfaces of MLG-114 and Ch-140 were determined by X-ray photoelectron spectroscopy (XPS) on freshly cleaved crystal fragments approximately 4×4×0.25 mm in size. The XPS analyses were performed at a base pressure of 10^{-7} Pa using non-monochromatic Al Kα photons from a Vacuum Generator XR3 double anode X-ray source (operated at 15 kV, 18 mA). Spectra were recorded with a double pass, cylindrical-mirror analyzer (PHI 15-255G) operated at a constant pass energy of 50 eV (spot size ~ 2 mm).

The binding energy (BE) scale was calibrated (Barr et al. 1997; Elmi et al. 2010; 2011; 2013) according to the C_{1s} signal of adventitious carbon (*i.e.* a common contaminant after the surface is exposed to air) on each sample (fixed at BE = 285.1 eV). Because of the high surface sensitivity of the XPS technique as determined by the inelastic mean free path of photoelectrons, the analysis was limited to a few nanometers (1-3 nm) with an elemental concentration greater than 0.1 atomic %. A preliminary identification of the elements included a fast survey scan (6 scans at pass energy of 100 eV) over an extended area which assured a sufficiently strong signal from the chemical species under evaluation.

Short sputtering of the sample surfaces was performed with an Argon ion gun under an accelerating voltage of 0.5 kV to remove any possible contaminant from the outermost layer. Each element on surfaces of both samples was measured after 30 min of Ar^+ sputtering in the region of Si_{2p}, Al_{2p}, Fe_{2p}, K_{2p}, Li_{1s}, and F_{1s} core levels. Opposite sides of a single mica flake, which were in contact before being cleaved, were studied for sample Ch-140. No severe charging effects that could possibly compromise data acquisition were observed.

Following a similar procedure as previously discussed in Elmi et al. (2010, 2011, 2013, 2014) a quantitative Si, Al, Fe, K, Li and F surface-chemical composition was derived from the photoionization peak areas (Muilenberg 1979) that considered the appropriate atomic sensitivity factors for each element. Chemical composition at the surface was normalized to 100% after adventitious carbon subtraction, according to the method introduced by Smith (2005), and then compared to bulk chemistry obtained by EMPA data.

RESULTS AND DISCUSSION

Mineral chemistry

The polylithionite (MLG-114) structural formula is $^{[XII]}(K_{0.952}Na_{0.019}Rb_{0.019})$ $^{[VI]}(Al_{1.034}Li_{1.459}Fe^{2+}_{0.389}Fe^{3+}_{0.046}Mn_{0.038}Mg_{0.002}Zn_{0.002}Ti_{0.001})$ $^{[IV]}(Al^{3+}_{0.477}Si_{3.523})O_{10.081}(F_{1.735}OH_{0.184})$ and the Fe-rich polylithionite (Ch-140) structural formula is $^{[XII]}(K_{0.992}Na_{0.014})$

Always consult and cite the final, published document. See http://www.minsocam.org or GeoscienceWorld

$^{[VI]}(Al_{0.980}Li_{1.028}Fe^{2+}_{0.787}Fe^{3+}_{0.022}Mn_{0.059}Mg_{0.052}Zn_{0.010}Ti_{0.024})$ $^{[IV]}(Al^{3+}_{0.857}Si_{3.143})$ $O_{10.095}$ $(F_{1.617}$ $OH_{0.288})$ (Table 1). MLG-114 lies in the polylithionite field (Tischendorf et al. 2007) and is similar to crystals described by Brigatti et al. (2000, 2007), and Mizota et al. (1986). Sample Ch-140 is located in composition near the polylithionite and siderophyllite fields and shows similar composition to some crystals described by Brigatti et al. (2000) (Fig. 1).

Chemical substitutions linking siderophyllite and polylithionite involve Li^{1+} for Fe^{2+} substitution in the octahedral sheet, which is charge balanced by Si^{4+} for Al^{3+} substitution in the tetrahedral sheet. This substitution is greater in MLG-114, which plots among the highest in Li+Si when compared to values in the literature, whereas sample Ch-140 shows significant, but yet much lower values (Fig. 2). MLG-114 and Ch-140 are characterized also by a significant F content in the anion site. F content increases with Li content, which is an indirect effect of an octahedral Fe decrease (F-Fe avoidance), thus accounting for the greater value observed in MLG-114 with respect to Ch-140 (Table 1).

Generally, Ti content is positively correlated to $^{[vi]}Fe^{2+}$ and negatively correlated to Li^{+}, thus indicating an increasing Li^{+} for Fe^{2+} substitution. This substitution generates a charge compensating substitution that involves the tetrahedral site over charge compensation mechanisms relating to the octahedral site only. This is consistent with only limited Ti content observed in the Ch-140 sample and no detectable Ti in the MLG-114 sample.

Bulk crystal chemistry and topology

Both crystals belong to space group *C*2 and are 1*M* polytypes (Table 2). Atomic positions of polylithionite-1*M* from Brigatti et al. (2000) were assumed as starting values. Appropriate neutral scattering factors were used for both cation and anion positions. In the final cycles of refinement, anisotropic displacement parameters were refined for all atoms. Final refinements yielded an agreement factor $R = 3.58\%$ for MLG-114 and $R = 3.75\%$ for Ch-140 (Table 2). The final atomic coordinates, displacement parameters, calculated bond lengths (Table 3), and important structural parameters (Table 4) are reported.

The effects of the $^{[vi]}Li_{-1}{}^{[iv]}Si_{-1}$ $^{[vi]}Fe^{2+}$ $^{[iv]}Al$ exchange vectors are evident with lateral cell dimensions decreasing as Si and Li increase. The MLG-114 sample is thus characterized by the smallest *a* and *b* values in the plot of Figure 3a, which includes previously reported Li, Fe-rich mica-1*M* with *C*2 symmetry in the polylithionite field or between the polylithionite and siderophyllite fields as defined by Tischendorf et al. (2007). Because of its effect over the tetrahedral composition, the effect of the polylithionite substitution is also related to the interlayer

Always consult and cite the final, published document. See http://www.minsocam.org or GeoscienceWorld

coordination, with the average distance of basal oxygen atoms from the interlayer cation decreasing with increasing Si content. In addition, the area of the hexagonal cavity is defined by the basal oxygen atoms (Fig. 3b; Table 5). The reduction in basal tetrahedral area is not related to the tetrahedral rotation angle (α), unlike what is commonly observed in 1*M* micas (Brigatti and Guggenheim 2002; Brigatti et al. 2011; Guggenheim 2011). If the polylithionite substitution increases, the average distance between basal tetrahedral oxygen atoms and the mean value of the octahedral unshared edge are both observed to decrease. These changes involve a reduction in strain in a 2:1 layer because opposing tetrahedral sheets are under tension. Reduction in basal oxygen distances reduces the tension and better achieves a near planar basal plane. This observation is also related to the concomitant decrease in the Al tetrahedral content, which progresses with Li substitution.

Both the T1 and T11 tetrahedra are elongated with the τ angle values varying from 111.2° to 112.0°, which are greater than the ideal 109.47° value. For MLG-114 and Ch-140 comparisons to samples from the literature, the plot shows that the effect of the polylithionite substitution produces a decrease in tetrahedral volume (Fig. 4a) and an increase in τ angle (Fig. 4b), primarily evident in the T1 tetrahedral site.

A significant feature of the Li-rich micas studied here is the difference in size and scattering efficiency between the octahedral M2 and M3 sites (Tables 1 and 5), which accounts for the reduction from *C*2/*m* to *C*2 in symmetry. Thus, three uniquely different cation sites occur in the octahedral sheet: M1, M2, and M3. For the studied crystals, M1 and M3 are similar in size and much larger than M2 (Table 3). The mean electron count (m.e.c.) determined for M1, M2 and M3 sites is M3 < M1 < M2 in the MLG-114 sample and M1 ≅ M2 < M3 in the Ch-140 sample. The mean electron counts determined for the M2 sites are close in both samples (m.e.c. $_{M2}$ = 12.78 for MLG-114 and m.e.c. $_{M2}$ = 12.87 for Ch-140), unlike M1 (m.e.c. $_{M1}$ = 9.84 for MLG-114 and m.e.c. $_{M1}$ = 12.71 for Ch-140) and M3 (m.e.c. $_{M3}$ = 7.81 for MLG-114 and m.e.c. $_{M3}$ = 13.53 for Ch-140). Based on mean electron counts, mean bond distances, and chemical analyses, Al preferentially occupies the M2 site, whereas Fe and Li are disordered between M1 and M3 sites with a slight preference of Fe for the M1 site (MLG-114) and for the M3 site (Ch-140). The effect of the polylithionite substitution on the octahedral sites is evident as well. In particular, the dimensions of the M1 and M3 sites decrease with Si increase, thus also accounting for the smallest values characterizing MLG-114 in Figure 5. The size of M2 is not significantly affected by polylithionite substitution. Figure 5 shows that the variance of unshared M2 edges increases with Li.

Always consult and cite the final, published document. See http://www.minsocam.org or GeoscienceWorld

Surface features

Because of possible charge effects, the binding energy (BE) of the C_{1s} level was obtained from saturated-hydrocarbon contamination at 285.1 eV, thus providing an internal standard for the calibration of each spectrum. The precision of BE values was estimated at ± 0.2 eV. A precise determination of each element on the crystal surfaces was obtained in the region of the Si_{2p}, Al_{2p}, Fe_{2p}, K_{2p}, Li_{1s}, and F_{1s} core levels. Experimental data are reported in plots representing the number of emitted electrons *vs.* their characteristic binding energies. XPS structures were fitted to Voigt peaks, after a Shirley background subtraction (Shirley 1972).

The Si_{2p} spectrum is shown in Figure 6. The deconvolution of the Si_{2p} spectra into individual components suggests the presence of two different types of Si sites: Si^{4+} (BE = 102.3 eV for MLG-114; BE = 102.4 for Ch-140) and Si^{1+} (BE = 99.4 eV for MLG-114 and BE = 99.3 for Ch-140) (Himpsel et al.1988). For both samples, the most prominent peak is assigned to Si^{4+} in tetrahedral coordination according to literature values obtained from other silicates (BE from 102.36 to 102.16 eV; Biino and Gröning 1998; Wagner et al. 1982; Bhattacharyya 1993 Hasha et al. 1988; Elmi et al. 2013, 2014). The cleavage mechanism, as determined from surface chemical composition, appears related to the breaking of bonds between the interlayer cation to tetrahedral-basal oxygen atoms, as indicated by a reduction of interlayer cation content at the surface with respect to the bulk (Table 6). Thus, tetrahedra (SiO_4) and Si cations show an excess of negative charge at the surface owing to the decrease of the number of interlayer cations after cleavage. This charge imbalance probably enhances the reactivity of the surface by creating an attraction, for example, of polar H_2O molecules after cleavage. In addition, this attraction will produce a reduced and/or distorted coordination of tetrahedral cations at the crystal surface. Spectral evidence for this is the small component at BE = 99.4 eV for MLG-114 and BE = 99.3 for Ch-140. Presumably, a limited number of Si ions with reduced coordination (< 4) exists as a consequence of these distortions.

The Fe_{2p} spectra are characterized by doublet structures relating to the spin orbit splitting between $2p_{1/2}$ and $2p_{3/2}$ states. The deconvolution of the $Fe_{2p3/2}$ peak (BE = 712.5 eV, in both samples) suggests two main components: one component is at BE of 710.7 eV and the second component is at BE = 713.1 eV (Fig. 7). The $Fe_{2p3/2}$ satellite peak at 716.0 eV is distinguishable and does not overlap either the $Fe_{2p3/2}$ or $Fe_{2p1/2}$ peaks. In addition, a peak occurs at 730.0 eV, which is a satellite peak for $Fe_{2p1/2}$. The deconvolution of the $Fe_{2p1/2}$ peak indicates that the two main components are Fe^{2+} (BE = 724.1 eV) and Fe^{3+} (BE = 726.6 eV).

Because of the inability to determine the contribution of each component following a Gauss-Voigt deconvolution procedure, the main $2p_{3/2}$ peak maximum at BE = 712.5 eV represents the

Always consult and cite the final, published document. See http://www.minsocam.org or GeoscienceWorld

summation of the Fe^{2+} and Fe^{3+} components. This result is similar to that observed for magnetite by Grosvenor et al. (2004).

For both samples here, the first component (label Fe^{2+}, Fig. 7) at BE = 710.7 eV is related to Fe^{2+} in octahedral coordination, similar to olivine $(Mg,Fe)_2SiO_4$, where the BE is reported at 710.8 eV (Seyama and Soma 1987) and iron oxide FeO (BE = 710.8 eV, Mills and Sullivan 1983). The second component (label Fe^{3+}, Fig. 7) at BE = 713.0 eV is related to Fe^{3+} in octahedral coordination (Grosvenor et al. 2004).

The Al_{2p} peak was located at BE = 74.4 eV for both samples, with no evident asymmetries in the peak shape (Fig. 8). The Al peak binding energy ranges from 74.19 to 74.63 eV for feldspars (Kyono et al. 2003) and from 74.2 to 75.3 eV for silico-alumino-phosphates (Hasha et al. 1988), in which Al is tetrahedrally coordinated. The Al binding energy is at 74.8, 74.3, and 74.0 eV in pyrophyllite (Barr et al. 1997), in kaolinite (Barr et al. 1997), and biotite (Ilton and Veblen 1994), respectively, where Al is mostly octahedrally coordinated. Aluminum is at BE = 74.1 eV in muscovite (Elmi et al. 2013), in which Al is present both in tetrahedral and octahedral coordination. Although in layer silicates the Al binding energy value is very close to both four-fold and six-fold coordination, the 74.4 eV value obtained for both polylithionite crystals may suggest a prevalent octahedral coordination. Barr et al. (1997) noted that in sheet silicates such as kaolinite, the positive nature of the octahedral sheet coupled with the relatively negative silicate layer results in more ionic Al–O bonds in kaolinite and allophane than in Al_2O_3. This increase in Al_{2p} binding energies found in layer minerals (such as kaolinite), should be enhanced in the case of the 2:1 minerals (such as pyrophyllite or smectite). This enhancement is related to an octahedral sheet that must compensate the charge of two relatively negative and adjacent tetrahedral sheets. The enhanced ionicity of the Al–O bond is reflected in the relatively higher Al_{2p} binding energy value for montmorillonite (74.8 eV). Barr et al. (1997) suggested also that the presence of OH and/or F enhances the positive character of the Al resulting in a moderate increase in the Al_{2p} binding energy (BE Al_{2p} for topaz is 74.6 eV).

The Li_{1s} core level appears at the binding energies of 55.4 eV (MLG-114) and 55.3 eV (Ch-140) (Fig. 9), which are more consistent with the LiF binding energy reported in the literature (BE range from 55.7 to 56.8 eV, Hamrin et al. 1970; Ro and Linton 1993), than with the binding energy for Li_2O (BE Li_2O = 53.9 eV; Tanaka et al. 2000). These values may indicate that the occurrence of Li cations in the octahedral sheet is preferentially associated with F^- over the OH^- groups (BE of LiOH = 54.9 eV; Contour et al. 1979).

Always consult and cite the final, published document. See http://www.minsocam.org or GeoscienceWorld

The F_{1s} peak appears at BE 685.5 and 685.7 eV for for MLG-114 and Ch-140, respectively (Fig. 10). Measured binding energies in LiF are very similar to those reported for F by several authors (BE from 685.0 eV to 686.5 eV, Hamrin et al. 1970; Ro and Linton, 1993; Verdier et al. 2007). The binding energy of Al_{2p} in polylithionites with respect to AlF_3 (BE = 77.1 eV; Hess et al. 1994) and $Al(OH)_3$ (BE = 74.2 eV; Hess et al. 1994) may suggest a preference of Al for OH. Because of the difficulties to separate the tetrahedral and octahedral contributions from the Al_{2p} spectrum, further investigations are required to confirm this detail.

The $K_{2p3/2}$ BE values are at 293.3 for both samples (Fig. 11). This measured value agrees well with those for phengitic muscovite (BE = 293.26 eV; Biino and Gröning 1998) and with those reported for sodian muscovite (BE = 293.3 eV; Elmi et al. 2013) and this result is consistent with an eight-fold coordination (Zakaznova-Herzov et al. 2008). Also in trioctahedral micas (Elmi et al. 2014), the K coordination is slightly lower at the surface than that observed in the bulk. The reduction at the surface of the interlayer cation coordination suggests a slight relaxation effect. Considering that the escape depth for all of the photoelectrons is ~15 Å at a pass energy of 100 eV, the reduction of the interlayer cation coordination, from nine to eight at the surface with respect to the bulk, may be an average of the outermost interlayer and the next interlayer that is deeper in the structure. This assumption suggests that the interlayer cation coordination is subjected to a reduction of coordination to six and then a slight relaxation occurs. Nevertheless, this suggestion requires further confirmation.

The chemical composition at the surface was normalized to 100%, after carbon subtraction (Smith 2005), and then compared to the bulk chemical composition determined by EMPA (Table 6). This comparison highlight, for both samples, a close similarity in chemical composition on the surface and in the bulk for Si. The XPS spectra seem to suggest, on the other hand, a decrease in K content and a strong increase in Li content close to the cleavage surface. The decrease in K content may be explained by its location on the cleavage surface, because the cation is expected to be distributed equally along the two surfaces generated upon cleavage. The potassium deficit observed comparing the MLG-114 and Ch-140 surfaces may be related to K loss because of the weaker K–OH or K–O bonds.

Although for other micas (*i.e.*, sodian muscovite, Elmi et al. 2013) there has been evidence indicating that the surface and bulk composition are closely similar, Evans et al. (1979) found a different composition between the bulk and the surface of phlogopite, vermiculite, and lithium phlogopite. Evans and Hiorns (1982) observed that chlorites also tend to cleave in regions of anomalous (non-bulk) composition. Moreover, Evans and Raftery (1982) found that in lepidolite,

Always consult and cite the final, published document. See http://www.minsocam.org or GeoscienceWorld

cleavage preferentially occurs in manganese-enriched regions. Manganese(II) occupies octahedral locations equivalent to those of Li. The increase in Li content, observed on both polylithionite surfaces, suggests a preference cleavage plane near lithium-enriched regions. Further explanation for this evident Li concentration increase is that the Li segregates from the Fe cations within M1 and M3 although in a random way (to conform to the X-ray refinement). The marked increase of Li together with the core level position of the Li_{1s} and F_{1s} peaks of both samples demonstrates that Li^{+} and F^{-} ions form domains in polylithionite.

For sample Ch-140, a pair of complementary cleaved surfaces, in contact before cleavage, were examined. Data reported in Table 6 indicate that the analyses for both Ch-140 pairs are approximately the same. Thus, the results indicate that about half of the interlayer cations remains on each surface.

IMPLICATIONS

Differences have been established between the bulk structure and the surface structure of two lithium micas to determine if the lithium content may play a role in cleavage, because most workers assume that cleavage is related to weaker bonds across the interlayer (regardless of bulk chemical composition). We were interested in seeing if Li content is an important influence in cleavage because Li ions tend to form domains in Li-rich micas, and the Li-O bonds also tend to be weak. More work is required to determine if Li content is important in the determination of cleavage. Thus, this work is the first step to understand the nature and magnitude of the surface energies, which play an important role in so many environmental and technological applications (*i.e.*, nanocomposites, biodegradable hybrid materials, and cosmetics).

ACKNOWLEDGMENTS

The authors acknowledge Fondazione Cassa di Risparmio di Modena (International Projects) and Ministero dell'Università e della Ricerca Scientifica of Italy (MIUR PRIN2010-2011) for supporting this research. This work benefitted from improvements after the revision process by the Associated Editor, Lynda Williams. We are grateful to Michael Henderson and an anonymous reviewer for insightful comments and suggestions.

REFERENCES

Backhaus, K.O. (1983) Structure refinement of a lepidolite-1M. Crystal Research Technology, 18, 253–1260

Always consult and cite the final, published document. See http://www.minsocam.org or GeoscienceWorld

Bailey, S.W. (1984) Crystal chemistry of the true micas. In: Micas (S.W. Bailey, ed.). Reviews in Mineralogy, 13, 13–60

Barr, T.L., Seal, S., Wozniak, K., and Klinowaki, J. (1997) ESCA studies of the coordination state of aluminum in oxide environments. Journal of the Chemical Society, Faraday Transactions, 93, 181–186. doi:10.1039/a604061f

Bhattacharyya, K.G. (1993) XPS study of mica surfaces. Journal of Electron Spectroscopy and Related Phenomena, 63, 289–306.

Biino, G.G., and Gröning, P. (1998) Cleavage mechanism and surface chemical characterization of phengitic muscovite and muscovite as constrained by X-Ray Photoelectron Spectroscopy. Physics and Chemistry of Minerals, 25, 168–181.

Brigatti, M.F., Lugli, C., Poppi, L., Foord, E.E., and Kile, D.E. (2000) Crystal chemical variations in Li- and Fe-rich micas from the Pikes Peak batholith (central Colorado). American Mineralogist, 85, 1275-1286.

Brigatti, M.F., and Guggenheim, S. (2002) Mica crystal chemistry and the influence of pressure, temperature, and solid solution on atomistic models. In Micas: crystal chemistry and metamorphic petrology (A. Mottana, F.P. Sassi, J.B.Jr. Thompson, S. Guggenheim, editors). Reviews in Mineralogy and Geochemistry, 46, Mineralogical Society of America and the Geochemical Society, Washington, D.C. (1–97).

Brigatti, M.F., Mottana, A., Malferrari, D., and Cibin, G. (2007) Crystal structure and chemical composition of Li-, Fe-, and Mn-rich micas. American Mineralogist, 92, 1395–1400

Brigatti, M.F., Malferrari, D., Laurora, A., and Elmi, C. (2011) Structure and mineralogy of layer silicates: recent perspectives and new trends. In: Layered mineral structures and their Application in Advanced Technologies (M.F. Brigatti and A. Mottana, editors). EMU Notes in Mineralogy, 11, The Mineralogical Society of Great Britain and Ireland (1–71). doi: 10.1180/EMU-notes.11.1

Bruker (2003) SMART and SAINT-Plus, version 6.01. Bruker AXS Inc., Madison, Wisconsin.

Cibin, G., Mottana, A., Marcelli, A., Cinque, G., Xu W., Wu, Z., and Brigatti, M.F. (2010) The interlayer structure of trioctahedral lithian micas: an AXANES spectroscopy study at the potassium K-edge. American Mineralogist, 95, 1084–1094. doi: 10.2138/am.2010.3344

Contour, J.P., Salesse, A., Froment, M., Garreau, M., Thevenin, J., and Warin, D. (1979) Electron microscopy and photoelectron spectroscopy analysis of lithium surfaces polarised in anhydrous organic electrolytes. Journal de Microscopie et de Spectroscopie Electroniques,4, 483-491

Always consult and cite the final, published document. See http://www.minsocam.org or GeoscienceWorld

Cundy, E.K., Windle, W., and Warren, I.H. (1960) the occurrence of zinnwaldite in Corwall. Clay Minerals Bulletin, 4, 151–156

Dornberger-Schiff, K., Backhaus, K.O., and Ďurovič, S. (1982) Polytypism of micas: OD-interpretation, stacking symbols, symmetry relations. Clays and Clay Minerals, 30, 364-374.

Elmi, C., Brigatti, M.F., Pasquali, L., Montecchi, M., Laurora, A., Malferrari, D., and Nannarone, S. (2010) Crystal chemistry, surface morphology and X-ray photoelectron spectroscopy of Fe-rich osumilite from Mt. Arci, Sardinia (Italy). Physics and Chemistry of Minerals, 37, 561–569. doi:10.1007/s00269-010-0357-4

Elmi, C., Brigatti, M.F., Pasquali, L., Montecchi, M., Laurora, A., Malferrari, D., and Nannarone, S. (2011) High-temperature vesuvianite: crystal chemistry and surface considerations. Physics and Chemistry of Minerals, 38, 459–468. doi: 10.1007/s00269-011-0419-2

Elmi, C., Brigatti, M.F., Guggenheim, S., Pasquali, L., Montecchi, M., Laurora, A., Malferrari, D., and Nannarone, S. (2013) Sodian muscovite-2M_1: crystal chemistry and surface features. Canadian Mineralogist, 51, 319–328. doi: 10.3749/canmin.51.1.000

Elmi, C., Brigatti, M.F., Guggenheim, S., Pasquali, L., Montecchi, M., and Nannarone, S. (2014) Crystal chemistry and surface configurations of two iron-bearing trioctahedral mica-1M polytypes. Clays and Clay Minerals, in press.

Evans, S., and Hiorns, A.G. (1982) Angle-resolved X-ray photoelectron studies of cleavage in chlorites. Clays and Clay Minerals, 44, 398–407.

Evans, S., and Raftery, E. (1982) X-ray photoelectron diffraction studies of lepidolites. Clay Minerals, 17, 443–452.

Evans, S., Adams, J.M., and Thomas, J.M. (1979) The surface structure and composition of layered silicate minerals: Novel insights from X-ray photoelectron diffraction, K-emission spectroscopy and cognate techniques. Philosophical Transactions of the Royal Society A, 292, 563–591.

Foley, S.F. (1989) Experimental constraints on phlogopites chemistry in lamproites: 2. the effect of pressure-temperature variations. European Journal of Mineralogy, 2, 327–341.

Grosvenor, A.P., Kobe, B.A., Biesinger, M.C., and McIntyre, N.S. (2004) Investigation of multiplet splitting of Fe_{2p} XPS spectra and bonding in iron compounds. Surface and Interface Analysis, 36, 1564–1574. doi:10.1002/sia.1984

Guggenheim, S. (1981) Cation ordering in lepidolite. American Mineralogist, 66, 1221-1232.

Guggenheim, S. (2011) An Overview of Order/Disorder in Hydrous Phyllosilicates. In: Layered mineral structures and their Application in Advanced Technologies (M.F. Brigatti and A.

Always consult and cite the final, published document. See http://www.minsocam.org or GeoscienceWorld

461 Mottana, editors), EMU Notes in Mineralogy, 11, The Mineralogical Society of Great Britain
462 and Ireland (72–111). doi: 10.1180/EMU-notes.11.2
463 Guggenheim, S., and Bailey, S.W. (1977) The refinement of zinnwaldite-1M in subgroup
464 symmetry. American Mineralogist, 62, 1158-1167.
465 Hamrin, K., Johansson, G., Gelius, U., Nordling, C., and Siegbahn, K. (1970) Valence Bands and
466 Core Levels of the Isoelectronic Series LiF, BeO, BN, and Graphite Studied by ESCA. Physica
467 Scripta, 1, 277. doi:10.1088/0031-8949/1/5-6/018
468 Hasha, D., de Saldarriaga, L., Saldarriaga, C., Hathway, P.E., Cox, D.F., and Davis, M. (1988)
469 Studies of silicoaluminophosphates with the sodalite structure. Journal of the American
470 Chemical Society, 110, 2127–2135. doi: 10.1021/ja00215a020
471 Henderson, C.M.B., Martin, J.S., and Mason, R.A. (1989) Compositional reactions in Li-micas
472 from S.W. England and France; an ion- and electron microprobe study. Mineralogical
473 Magazine, 53, 627-669.
474 Hess, A., Kemnitz, E., Lippitz, A., Unger, W.E.S., and Menz, D.-H. (1994) ESCA, XRD, and IR
475 characterization of aluminum oxide, hydroxyfluoride, and fluoride surfaces in correlation with
476 their catalytic activity in heterogeneous halogen exchange reactions. Journal of Catalysis, 148,
477 270–280.
478 Himpsel, F.J., McFeely, F.R., Taleb-Ibrahimi, A., Yarmoff, J.A., and Hollinger, G. (1988)
479 Microscopic structure of the silica/silicon interface. Physical Review B: Condensed Matter and
480 Materials Physics, 38, 6084–6096. doi:10.1103/PhysRevB.38.6084
481 Hochella, M.F., Jr (1995) Mineral surfaces: their characterization and their chemical, physical and
482 reactive nature. In: Mineral surfaces (D.J. Vaughan and R.A.D. Pattrick, editors), The
483 Mineralogical Society Series 5 (17–60)
484 Ilton, E.S., and Veblen, D.R. (1994) Chromium sorption by phlogopite and biotite in acidic
485 solutions at 25 °C: insights from X-ray photoelectron spectroscopy and electron microscopy.
486 Geochimica and Cosmochimica Acta, 58, 2777–2788.
487 Kyono, A., Kimata, M., and Hatta, T. (2003) Aluminum position in Rb-feldspar as determined by
488 X-ray photoelectron spectroscopy. Naturwissenschaften, 90, 414–418. doi:10.1007/s00114-
489 003-0453-0
490 Maurice, P.A. (2009) Environmental Surfaces and Interfaces. From the nanoscale to the global
491 scale. John Wiley&Sons, Ltd., 441 pp.

Always consult and cite the final, published document. See http://www.minsocam.org or GeoscienceWorld

Meyrowitz, R. (1970) New semi micro procedure for determination of ferrous iron in refractory silicate minerals using a sodium metafluoborate decomposition. Analytical Chemistry, 42, 1110–1113.

Mills, P., and Sullivan, J.L. (1983) A study of the core level electrons in iron and its three oxides by means of X-ray photoelectron spectroscopy. Journal of Physics D: Applied Physics, 16, 723 doi:10.1088/0022-3727/16/5/005

Mitropoulos, P., Katerinopoulos, A., and Kokkinakis, A. (1999) Occurrence of primary almandine-spessartine-rich garnet and zinnwaldite phenocrysts in a Neogene rhyolite on the island of Chios, Aegean Sea, Greece. Mineralogical Magazine, 63, 503–510

Mizota, T., Kato, T., and Harada, K. (1986) The crystal structure of masutomilite, manganese analog of zinnwaldite. Mineralogical Journal (Japan), 13, 13–21.

Muilenberg, G.E. (Editor) (1979) Handbook of X-ray photoelectron spectroscopy. Physical Electronics Division, Perkin–Elmer Corp., Norwalk.

Pini, S., Brigatti, M.F., Affronte, M., Malferrari, D., and Marcelli, A. (2012) - Magnetic behavior of trioctahedral micas with different octahedral Fe ordering. Physics and Chemistry of Minerals, 39, 665–674.

Rieder, M., Cavazzini, G., D′yakonov, Y.S., Frank-Kamenetskii, V.A., Gottardi, G., Guggenheim, S., Koval, P.V., Müller, G., Neiva, A.M.R., Radoslovich, E.W., Robert, J.-L., Sassi, F.P., Takeda, H., Weiss, Z., and Wones, D.R. (1998) Nomenclature of the micas. Clays and Clay Minerals, 41, 61-72.

Ro, C., and Linton, R.W. (1993) Characterization of LiF using XPS. Surface Science Spectra, 1, 277-284. http://dx.doi.org/10.1116/1.1247651

Robert, J.-L., and Volfinger, M. (1979) Etude experimental de lepidolites hydroxyldes. Bulletin minéralogie, l02, 2l

Robert, J.-L., Bény, J.-M., Della Ventura, G., and Hardy, M. (1993) Fluorine in micas: crystal – chemical control of the OH-F distribution between trioctahedral and dioctahedral sites. European Journal of Mineralogy, 5, 7-18.

Seyama, H., and Soma, M. (1987) Fe_{2p} spectra of silicate minerals. Journal of Electron Spectroscopy and Related Phenomena, 42, 97–101. doi: 10.1016/0368-2048(87)85010-7

Sheldrick, G.M. (1996) SADABS. University of Göttingen, Germany.

Sheldrick, G.M. (1997) SHELXL97. Program for the Refinement of Crystal Structures. University of Göttingen, Germany.

Always consult and cite the final, published document. See http://www.minsocam.org or GeoscienceWorld

Shirley, D.A. (1972) Effect of atomic and extra-atomic relaxation on atomic binding energies. Chemical and Physical Letters, 16, 220–5. doi:10.1016/0009-2614(72)80260-4

Smith, G.C. (2005) Evaluation of a simple correction for the hydrocarbon contamination layer in quantitative surface analysis by XPS. Journal of Electron Spectroscopy and Related Phenomena, 148, 21–28. doi: 10.1016/j.elspec.2005.02.004

Tanaka, S., Taniguchi, M., and Tanigawa, H (2000) XPS and UPS studies on electronic structure of Li_2O. Journal of nuclear materials, 283-287, 1405–1408.

Tenório Cavalcante, P.M., Dondi, M., Guarini, G., Barros, F.M., and Benvindo da Luz, A. (2007) Ceramic application of mica titania pearlescent pigments. Dye Pigment, 74, 1–8. doi:10.1016/j.dyepig.2006.01.026

Tischendorf, G., Fo□rster, H.-J., Gottesmann, B., and Rieder, M. (2007) True and brittle micas: composition and solid-solution series. Mineralogical Magazine, 71, 285–320. DOI: 10.1180/minmag.2007.071.3.285

Verdier, S., El Ouatani, L., Dedryvère, R., Bonhomme, F., Biensan, P., and Gonbeau, D. (2007) XPS study on Al_2O_3- and $AlPO_4$-coated $LiCoO_2$ cathode material for high-capacity Li ion batteries. Journal of The Electrochemical Society, 154, A1088-A1099. doi: 0013-4651/2007/154(12)/A1088/12/

Wagner, C.D., Passoja, D.E., Hillery, H.F., Kinisky, T.G., Six, H.A., Jansen, W.T., and Taylor, J.A. (1982) Auger and photoelectron line energy relationship in aluminum-oxygen and silicon-oxygen compounds. Journal of Vacuum Science and Technology, 21, 933–944.

Zakaznova-Herzog, V.P., Nesbesbesbitt, H.W., Bancroft, G.M., and Tse, J.S. (2008) Characterization of leached layers on olivine and pyroxenes using high-resolution XPS and density functional calculations. Geochimica et Cosmochimica Acta, 72, 69–86. doi: 10.1016/j.gca.2007.09.031

Figures/captions

Always consult and cite the final, published document. See http://www.minsocam.org or GeoscienceWorld

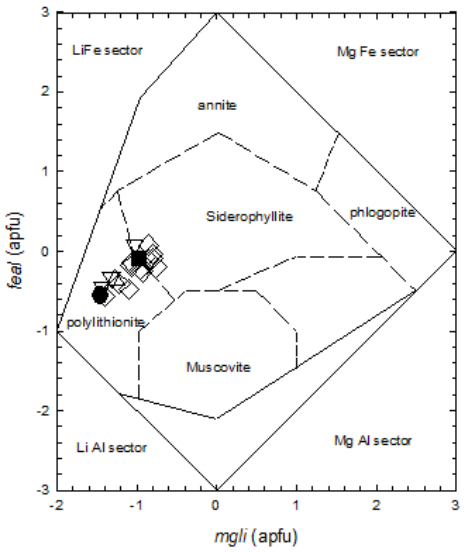

Figure 1

551

552 **Figure 1.** Li-rich micas based on the classification diagram after Tischendorf et al. (2007). *mgli* =

553 (Mg - Li); *feal* = (Fe_{Tot} + Mn + Ti - $^{[vi]}$Al). Symbols: filled circle: MLG-114, this study; filled

554 square: Ch-140, this study; open symbols: Samples from literature (triangle down = Brigatti et al.

555 2007; diamond = Brigatti et al. 2000; triangle up = Mizota et al. 1986).

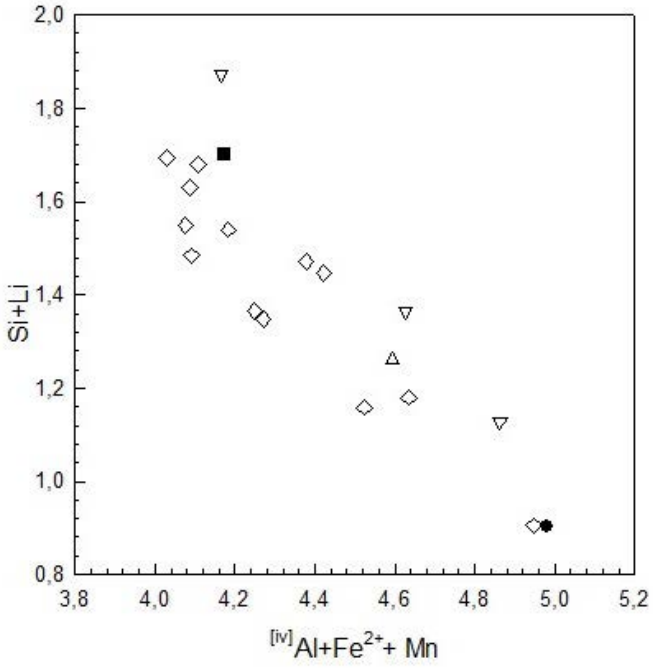

556

Always consult and cite the final, published document. See http://www.minsocam.org or GeoscienceWorld

557 **Figure 2.** Variation of $^{[iv]}Al^{3+}+ {}^{[vi]}Fe^{2+}+{}^{[vi]}Mn^{2+}$ content with $^{[iv]}Si+ {}^{[vi]}Li$ content. All symbols are as

558 in Figure 1.

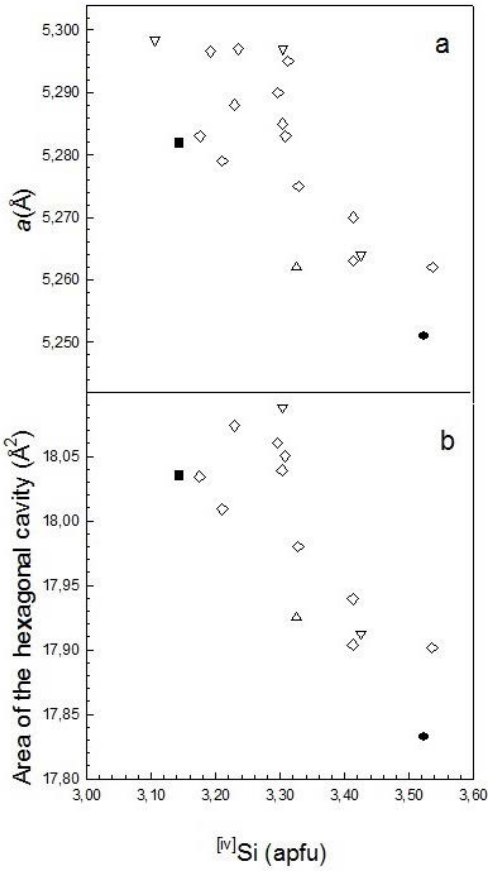

559

560 **Figure 3.** Variation of **(a)** unit cell parameter *a* and **(b)** area of tetrahedral hexagonal cavity with Si

561 content. All symbols are as in Figure 1.

Always consult and cite the final, published document. See http://www.minsocam.org or GeoscienceWorld

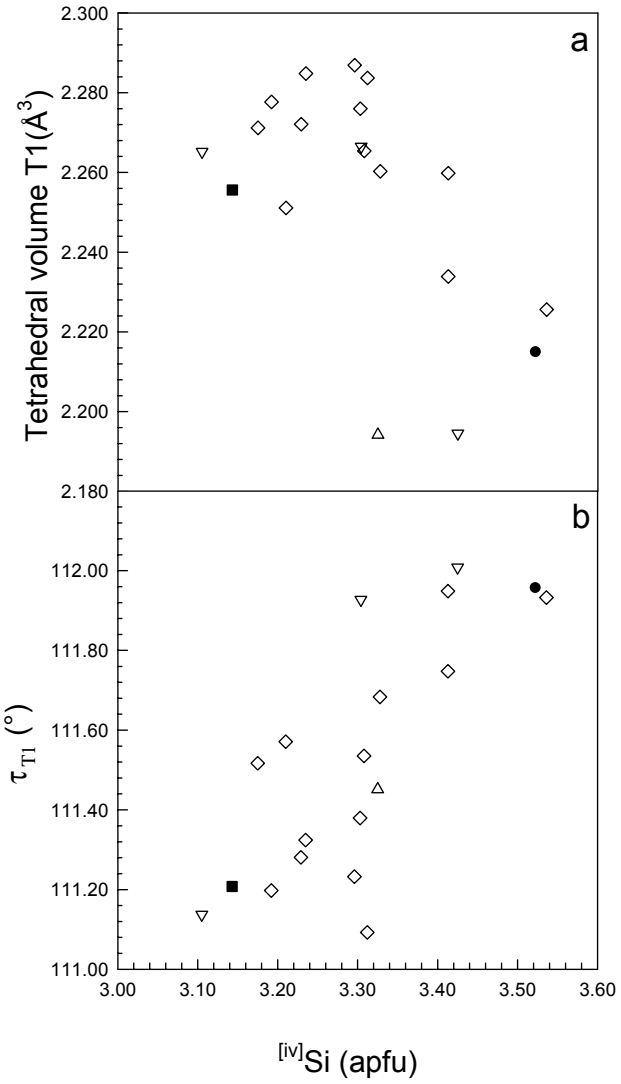

Figure 4 (a,b)

Figure 4. Variation of tetrahedron T1 parameters with [iv]Si. **(a)** tetrahedral volume; **(b)** tetrahedral flattening angle τ. All symbols are as in Figure 1.

Always consult and cite the final, published document. See http://www.minsocam.org or GeoscienceWorld

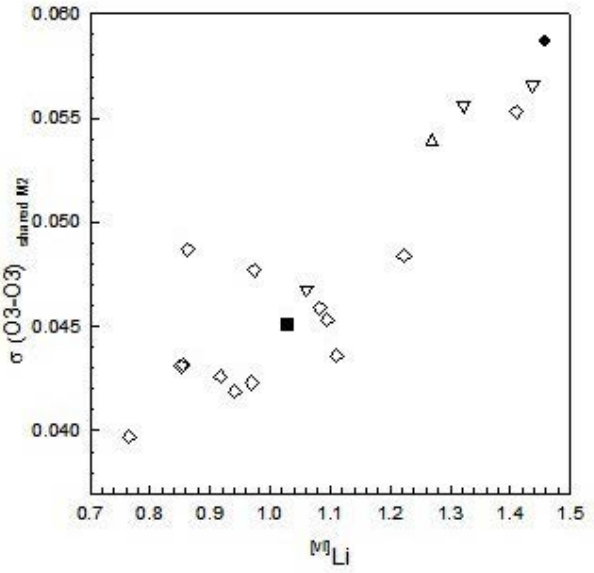

Figura 5. Relationships between the variance of unshared O3-O3 edges of M2 with Li. All symbols are as in Figure 1.

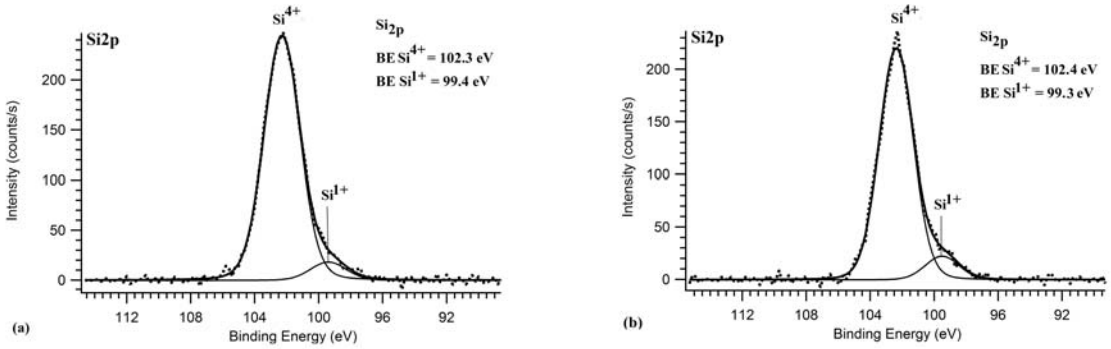

a **b**

Figure 6. Si_{2p} spectrum of MLG-114 **(a)** and Ch-140 **(b)** displayed as a plot of electron binding energy *vs*. intensity (the number of electrons per second in a fixed and small energy interval). The Si^{4+} and Si^{1+} peaks are labeled on the spectrum.

Always consult and cite the final, published document. See http://www.minsocam.org or GeoscienceWorld

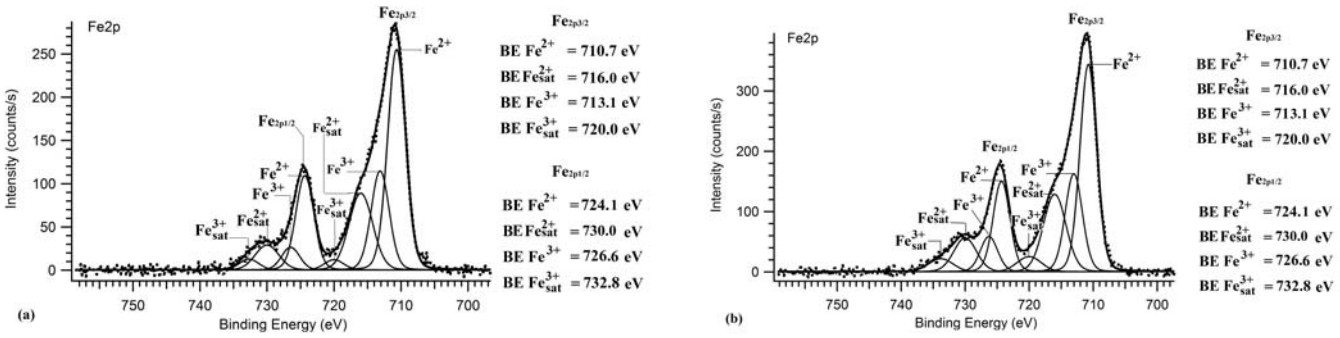

a **b**

574 **Figure 7. (a)** Fe_{2p} spectrum with the curve fit obtained for MLG-114. The spectrum is displayed as
575 a plot of electron binding energy *vs*. intensity (the number of electrons per second in a fixed and
576 small energy interval). The Fe^{3+} and Fe^{2+} multiplet peaks are labeled on the spectrum. $Fe^{3+}{}_{sat}$ and
577 $Fe^{2+}{}_{sat}$ refer to the associated satellite peaks of Fe^{3+} and Fe^{2+}, respectively. **(b)** Fe_{2p} spectrum
578 obtained for Ch-140.

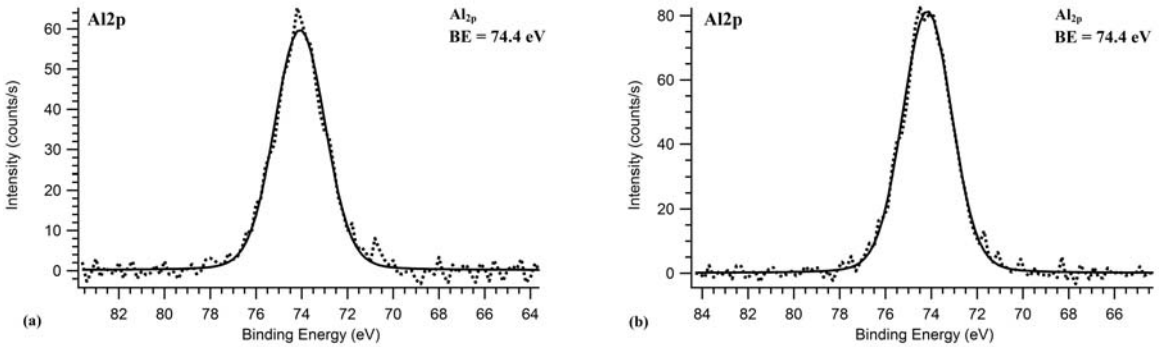

a **b**

579 **Figure 8.** Al_{2p} spectra of MLG-114 **(a)** and Ch-140 **(b)** displayed as a plot of electron binding
580 energy *vs*. intensity (the number of electrons per second in a fixed and small energy interval).

Always consult and cite the final, published document. See http://www.minsocam.org or GeoscienceWorld

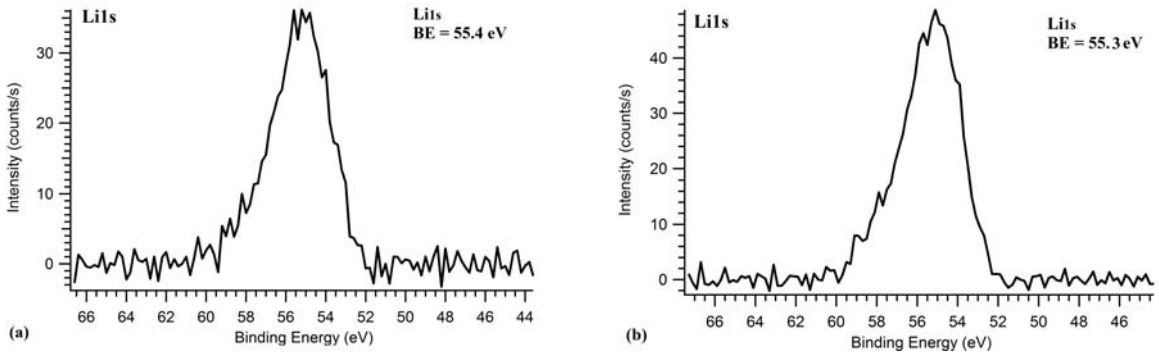

a **b**

581 **Figure 9.** Li_{1s} spectra of MLG-114 **(a)** and Ch-140 **(b)** displayed as a plot of electron binding
582 energy *vs*. intensity (the number of electrons per second in a fixed and small energy interval).

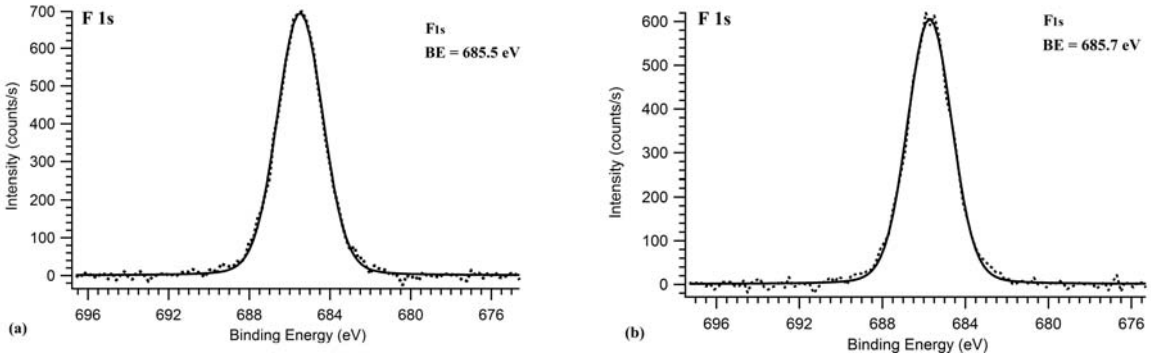

a **b**

583 **Figure 10.** F_{1s} spectra of MLG-114 **(a)** and Ch-140 **(b)** displayed as a plot of electron binding
584 energy *vs*. intensity (the number of electrons per second in a fixed and small energy interval).

Always consult and cite the final, published document. See http://www.minsocam.org or GeoscienceWorld

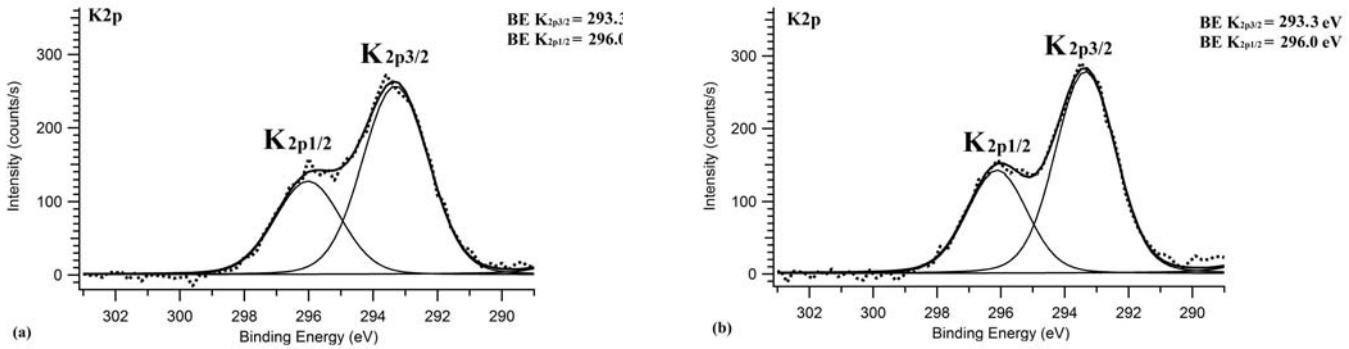

a **b**

585 **Figure 11.** K_{2p} spectra of MLG-114 **(a)** and Ch-140 **(b)** displayed as a plot of electron binding
586 energy *vs*. intensity (the number of electrons per second in a fixed and small energy interval).

587

Always consult and cite the final, published document. See http://www.minsocam.org or GeoscienceWorld

588 **Table 1**. Chemical data for polylithionite-1*M* crystals. Standard deviation in parenthesis.

Sample	MLG-114	Ch-140		MLG-114	Ch-140
	wt%			Atoms per formula unit (apfu)	
SiO_2	51.19 (0.83)	43.63 (0.75)	$^{[iv]}Si$	3.523	3.143
TiO_2	0.02 (0.01)	0.45 (0.04)	$^{[iv]}Al$	0.477	0.857
Al_2O_3	18.63 (0.42)	21.64 (0.38)	$^{[iv]}\sum$	4.000	4.000
Fe_2O_3	0.89	0.40	$^{[vi]}Al$	1.034	0.980
FeO	6.76 (0.12)	13.06 (0.21)	$^{[vi]}Ti^{4+}$	0.001	0.024
MgO	0.02 (0.01)	0.48 (0.12)	$^{[vi]}Fe^{3+}$	0.046	0.022
MnO	0.65 (0.14)	0.96 (0.12)	$^{[vi]}Fe^{2+}$	0.389	0.787
ZnO	0.04 (0.02)	0.19 (0.06)	$^{[vi]}Zn^{2+}$	0.002	0.010
Li_2O	5.27 (0.46)	3.55 (0.28)	$^{[vi]}Mn^{2+}$	0.038	0.059
Na_2O	0.14 (0.04)	0.10 (0.02)	$^{[vi]}Mg$	0.002	0.052
K_2O	10.85 (0.13)	10.80 (0.11)	$^{[vi]}Li$	1.459	1.028
Rb_2O	0.44 (0.05)	b.d.l.	$^{[vi]}\sum$	2.971	2.962
H_2O	0.4	0.6	$^{[xii]}Na$	0.019	0.014
F	7.97 (0.47)	7.10 (0.51)	$^{[xii]}K$	0.952	0.992
F = O	-3.35	-2.99	$^{[xii]}Rb$	0.019	
Σ	99.92	99.97	$^{[xii]}\sum$	0.99	1.006
			F	1.735	1.617
			OH	0.184	0.288
			O	10.081	10.095
			∑	12.000	12.000

589

590

Always consult and cite the final, published document. See http://www.minsocam.org or GeoscienceWorld

591 **Table 2.** Crystal, experimental, and refinement data for polylithionite-1*M* crystals.

	MLG-114	Ch-140
Space group	*C*2	*C*2
a (Å)	5.251(1)	5.282 (1)
b (Å)	9.066(2)	9.121(3)
c (Å)	10.087(2)	10.080(3)
β(°)	100.694(5)	100.764(5)
Cell volume (Å^3)	471.9(2)	477.1(2)
Crystal size (mm)	0.20×0.18×0.03	0.22×0.16×0.04
θ range (°)	4 to 30	4.1 to 32.3
Total reflections	1323	1680
Unique reflections	861	1056
$R_{(int)}$ (%)	1.93	2.63
Reflections used	861	1056
No. of refined parameters	98	100
GooF	1.021	0.996
R_1 (%) [I>2σ(I)]	3.58	3.75
wR_2 (on F^2)	7.25	6.91
$\Delta\rho_{min}$ (e/Å^3)	-0.405	-0.58
$\Delta\rho_{max}$ (e/Å^3)	0.606	0.55

Notes: $R1=\frac{\sum\|F_o|-|F_c\|}{\sum|F_o|}$; $wR^2=\left[\frac{\sum w\left(F_o^2-F_c^2\right)^2}{\sum w\left(F_o^2\right)^2}\right]^{1/2}$; GOF = $\left[\frac{\sum w\left(F_o^2-F_c^2\right)^2}{(n-p)}\right]^{1/2}$

$w = 1/[\sigma^2(F_O^2) + (a \times P)^2 + b \times P]$, where a = 0.0417, b = 0 for MLG-114 and a = 0.0287, b = 0 for Ch-140. $P = [(\max(F_O^2,0) + 2 \times F_C^2)]/3$; *n* is the number of reflections and *p* is the number of parameters refined.

592
593

Always consult and cite the final, published document. See http://www.minsocam.org or GeoscienceWorld

Table 3. Bond distances (Å) for Fe-polylithionite-1*M* crystals [space group *C*2; layer symmetry *C*121(1)]. Estimated standard deviations in parenthesis.

	MLG-114	Ch-140		MLG-	Ch-140		MLG-114	Ch-140
Tetrahedron T(1)			Octahedron			Interlayer cation		
T1-O1	1.641(6)	1.635(7)	M1-O3 (×2)	2.108(7)	2.155(7)	A-O1 (×2)	3.047 (3)	3.037(3)
T1-O2	1.639(5)	1.648(6)	M1-O33 (×2)	2.128(6)	2.115(7)	A-O1' (×2)	3.212(3)	3.246(3)
T1-O22	1.632(5)	1.647(6)	M1-O4 (×2)	2.120(3)	2.132(3)	A-O2 (×2)	3.052(5)	3.036(6)
T1-O3	1.606(5)	1.628(6)	<M1-O>	2.119	2.134	A-O2' (×2)	3.207(5)	3.237(7)
<T1-O>	1.630	1.639				A-O22 (×2)	3.007(5)	3.005(6)
Tetrahedron (T11)			Octahedron			A-O22' (×2)	3.130(5)	3.149(7)
T11-O1	1.626(6)	1.641(7)	M2-O3 (×2)	1.922(7)	1.891(6)	$<A\text{-}O>_{inner}$	3.035	3.027
T11-O2	1.630(5)	1.635(6)	M2-O33 (×2)	1.898 (4)	1.912(5)	$<A\text{-}O>_{outer}$	3.183	3.211
T11-O22	1.637(5)	1.632(6)	M2-O4 (×2)	1.831 (4)	1.873(5)			
T11-O33	1.623(5)	1.626(6)	<M2-O>	1.884	1.892			
<T11-O>	1.629	1.634	Octahedron					
			M3-O3 (×2)	2.115 (4)	2.133(5)			
			M3-O33 (×2)	2.108 (7)	2.152(7)			
			M3-O4 (×2)	2.138 (5)	2.124(5)			
			<M3-O>	2.120	2.136			

Always consult and cite the final, published document. See http://www.minsocam.org or GeoscienceWorld

597 **Table 4**. Crystallographic coordinates and equivalent isotropic displacement parameters ($Å^2 \times 10^3$). $U_{(eq)}$ is defined as one third of the
598 trace of the orthogonalized Uij tensor.

599

	x	y	z	$U_{(eq)}$	U_{11}	U_{22}	U_{33}	U_{23}	U_{13}	U_{12}
MLG-114 (Space group: *C*2)										
O(1)	0.0425(6)	0.9988(7)	0.1718(3)	17(1)	24(2)	13(1)	13(2)	5(3)	-1(1)	3(2)
O(2)	0.3192(9)	0.2417(5)	0.1728(6)	21(1)	11(2)	24(3)	26(4)	-4(2)	-1(2)	-3(2)
O(22)	0.8154(9)	0.2574(5)	0.1612(6)	16(1)	20(2)	18(3)	11(3)	0(2)	4(2)	4(2)
O(3)	0.1147(8)	0.1703(6)	0.3920(5)	13(1)	3(2)	12(2)	23(3)	-2(2)	1(2)	-2(2)
O(33)	0.6622(7)	0.3237(6)	0.3928(4)	9(1)	4(2)	6(2)	16(2)	-2(2)	2(1)	4(2)
O4	0.1100(5)	0.4691(3)	0.3993(2)	13(1)	13(2)	9(2)	16(2)	1(1)	1(1)	-3(1)
M1	0	0.9907(5)	0.5	11(1)	8(1)	6(2)	19(2)	0	0(1)	0
M2	0	0.3223(4)	0.5	11(1)	5(1)	12(1)	15(2)	0	-1(1)	0
M3	0.5	0.1599(6)	0.5	8(2)	6(3)	7(3)	10(3)	0	0(2)	0
T1	0.0762(3)	0.1680(1)	0.2303(2)	12(1)	6(1)	9(1)	20(1)	-2(1)	2(1)	0(1)
T2	0.5861(3)	0.3314(1)	0.2294(2)	12(1)	11(1)	7(1)	18(1)	0(1)	1(1)	0(1)
A	0	0.5009(3)	0	24(1)	24(1)	21(1)	27(1)	0	2(1)	0

Always consult and cite the final, published document. See http://www.minsocam.org or GeoscienceWorld

600
601
602

	x	y	z	$U_{(eq)}$	U_{11}	U_{22}	U_{33}	U_{23}	U_{13}	U_{12}
Ch-140 (Space group: *C*2)										
O(1)	0.0376(5)	0.9992(8)	0.1717(3)	20(1)	29(2)	10(2)	17(2)	-2(3)	-2(1)	2(3)
O(2)	0.3214(11)	0.2386(6)	0.1718(6)	20(1)	23(3)	21(3)	19(3)	1(2)	9(2)	-7(2)
O(22)	0.8134(11)	0.2589(6)	0.1604(6)	21(1)	17(2)	22(3)	23(3)	4(2)	0(2)	7(2)
O(3)	0.1135(9)	0.1744(6)	0.3919(6)	12(1)	11(2)	3(3)	21(3)	-2(2)	5(2)	2(2)
O(33)	0.6615(9)	0.3261(7)	0.3921(5)	12(1)	10(2)	13(2)	11(2)	-1(2)	0(2)	-3(2)
O4	0.1101(5)	0.4711(4)	0.3974(3)	20(1)	23(2)	15(3)	24(2)	4(2)	6(1)	-1(1)
M1	0	0.9892(4)	0.5	9(1)	11(1)	3(1)	14(1)	0	3(1)	0
M2	0	0.3209(4)	0.5	6(1)	5(1)	3(1)	10(2)	0	0(1)	0
M3	0.5	0.1572(3)	0.5	12(1)	13(1)	6(2)	17(2)	0	2(1)	0
T1	0.0746(4)	0.1675(1)	0.2280(2)	8(1)	9(2)	1(2)	13(2)	1(1)	1(1)	1(1)
T2	0.5850(4)	0.3309(2)	0.2282(2)	11(1)	9(1)	9(2)	16(2)	0(1)	3(1)	1(1)
A	0	0.5004(4)	0	29(1)	30(1)	21(1)	35(1)	0	5(1)	0

Always consult and cite the final, published document. See http://www.minsocam.org or GeoscienceWorld

603 **Table 5**. Selected parameters derived from structure refinement for MLG-114 and Ch-140 crystals.

604

605

	MLG-114	Ch-140
Tetrahedral parameters		
α (°)	3.3	4.1
Δz (Å)	0.1150	0.1109
τ_{T1} (°)	112.0	111.2
τ_{T11} (°)	111.7	111.4
$\langle A\text{- }O\rangle_{basal}$	3.109	3.119
$\langle O\text{-}O\rangle_{basal}$	2.627	2.645
Hexagonal cavity area (Å^2)	17.83	18.04
Tetrahedral basal area T1 (Å^2)	2.992	3.042
Tetrahedral basal area T11 (Å^2)	2.978	3.011
Octahedral parameters		
ψ_{M1} (°)	60.5	60.5
ψ_{M2} (°)	56.4	56.2
ψ_{M3} (°)	60.5	60.5
m.e.c.$_{M1}$	9.85	12.71
m.e.c.$_{M2}$	12.78	12.87
m.e.c.$_{M3}$	7.81	13.52
Layer thickness (Å)		
Tetrahedral (Å)	2.241	2.237
Octahedral (Å)	2.087	2.103
Interlayer (Å)	3.342	3.327

Always consult and cite the final, published document. See http://www.minsocam.org or GeoscienceWorld

606 **Table 6**. Results of quantitative analyses on MLG-114 and Ch-140a and Ch-140b by XPS
607 compared to EPMA data. Calculated ratio (wt.%) of the elements present at the polylithionite
608 surfaces are corrected using the method described by Smith (2005).

609

			Si	Al	K	**Li**	Fe	**F**	O
MLG-114	surface		20.76	7.18	5.67	**4.68**	2.87	**9.40**	49.44
	bulk		23.10	9.52	8.69	**2.36**	5.67	**7.69**	41.57
Ch-140	surface	(a)	17.55	9.38	5.63	**6.36**	4.13	**7.63**	49.33
		(b)	17.64	9.20	5.27	**6.59**	3.79	**6.92**	50.59
	bulk		19.81	11.13	8.71	**1.60**	10.13	**6.90**	40.17

610

Always consult and cite the final, published document. See http://www.minsocam.org or GeoscienceWorld